ACS OMEGA

Open Access

http://pubs.acs.org/journal/acsodf

Article

Nanorod-like Bimetallic Oxide for Enhancing the Performance of Supercapacitor Electrodes

Meilong Wang, Linsong Li, Zhentao Liu, Fuzhong Wu, Huixin Jin,* and Yi Wang*

Cite This: *ACS Omega* 2024, 9, 16118−16127

Read Online

ACCESS | Metrics & More | Article Recommendations | Supporting Information

ABSTRACT: Supercapacitors are widely used in many fields owing to their advantages, such as high power, good cycle performance, and fast charging speed. Among the many metal-oxide cathode materials reported for supercapacitors, $NiMoO_4$ is currently the most promising electrode material for high-specific-energy supercapacitors. We have employed a rational design approach to create a nanorod-like $NiMoO_4$ structure, which serves as a conductive scaffold for supercapacitors; the straightforward layout has led to outstanding results, with nanorod-shaped $NiMoO_4$ exhibiting a remarkable capacity of 424.8 F g^{-1} at 1 A g^{-1} and an impressive stability of 80.2% capacity preservation even after 3500 cycles, which surpasses those of the majority of previously reported $NiMoO_4$ materials. $NiMoO_4$//AC supercapacitors demonstrate a remarkable energy density of 46.31 W h kg^{-1} and a power density of 0.75 kW kg^{-1}. This synthesis strategy provides a facile method for the fabrication of bimetallic oxide materials for high-performance supercapacitors.

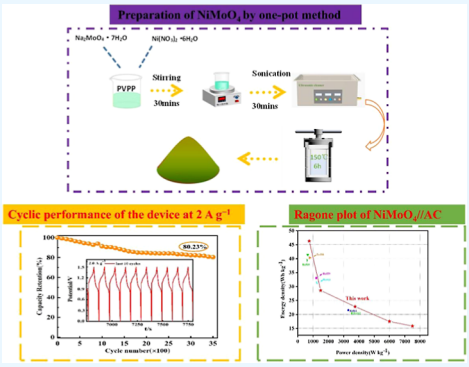

1. INTRODUCTION

In view of increasing environmental pollution, researchers have attempted to create eco-friendly energy storage systems that aim to fulfill the requirements of hybrid and portable electronic devices.[1−3] The scientific community has shown significant interest in supercapacitors owing to their notable benefits such as fast charge/discharge rates, long cycle lifetimes, high power density, and long-term stability.[4−8] Nevertheless, supercapacitors must be enhanced to align with market demands while preserving their inherent advantages. Extensive studies have shown that enhancing the capacitance and widening the potential range can enhance the energy storage capacity of supercapacitors.[9−11] Furthermore, nanostructured and multicomponent composite materials can enhance electrode specific capacitance; thus, nanostructures incorporating transition metal oxides (TMOs) or transition metal sulfides are a promising approach for high-performance electrodes.[12−14]

TMOs have gained popularity as electrode materials for supercapacitors owing to their high theoretical specific capacities, affordability, and outstanding chemical stabilities. Some notable TMOs include NiO,[15] Co_3O_4,[16−19] and MnO_2.[20] However, compared to single-metal oxides, bimetallic oxides are preferred because of their higher specific capacitance and electrical conductivity. This has led to the exploration of multiple metal oxides such as $ZnCo_2O_4$,[21] $NiCo_2O_4$,[22,23] $NiMoO_4$,[24] and $NiMn_2O_4$,[25] which have garnered considerable attention. Numerous studies have been conducted on $NiMoO_4$ because it is abundant in the Earth's crust.[26] Meanwhile, the particle size and shape, crystallinity, crystal structure, and porosity greatly influence $NiMoO_4$ electrochemical performance.[27−29,31] Despite this, $NiMoO_4$'s limited electrochemical active surface area makes its electrochemical performance unsatisfactory.[32] Hence, it is crucial to utilize an economical and simple fabrication technique to generate a structure with ample active surface area, thereby boosting the efficiency of $NiMoO_4$.[30]

The present investigation involved the synthesis of $NiMoO_4$ materials with nanorod-like structures through a one-pot hydrothermal technique. These materials were then examined for their suitability as electrode materials for supercapacitors. Significantly, the inclusion of $NiMoO_4$ nanorods greatly improved the capacitance, increasing it from 11 F g^{-1} (for NiO) to 424.8 F g^{-1} at 1 A g^{-1}. In addition, the device, which is equivalent to 0.75 kW kg^{-1}, exhibited an impressive energy density of 46.31 W h kg^{-1}. Moreover, it displayed outstanding stability throughout 3500 GCD cycles, retaining 80.2% of its capacitance. The rapid movement of electrons and ions in the $NiMoO_4$ nanorods' distinct nanostructure is responsible for their improved performance, setting them apart from other nanostructured $NiMoO_4$ materials and showcasing their potential for effective energy storage. As a result of the synthesis strategy, a high-performance supercapacitor is fabricated with nano crystalline bimetallic oxide material.

Received: December 13, 2023
Revised: March 10, 2024
Accepted: March 18, 2024
Published: March 28, 2024

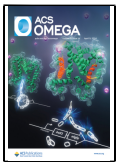

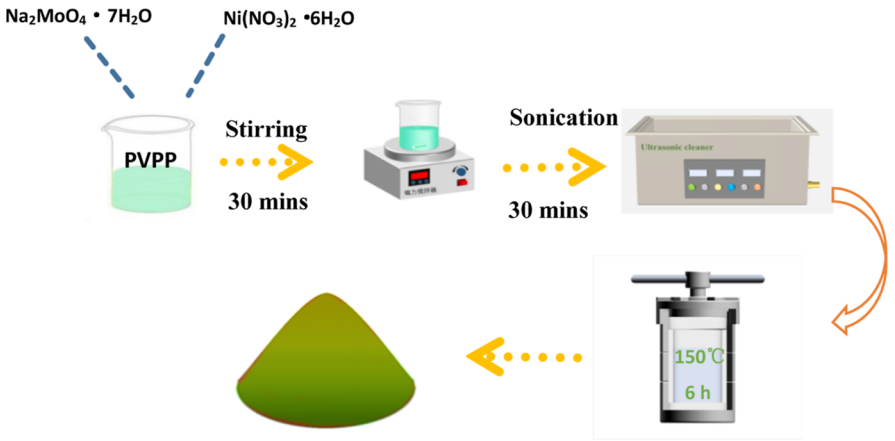

Figure 1. Preparation of $NiMoO_4$ schematic illustration.

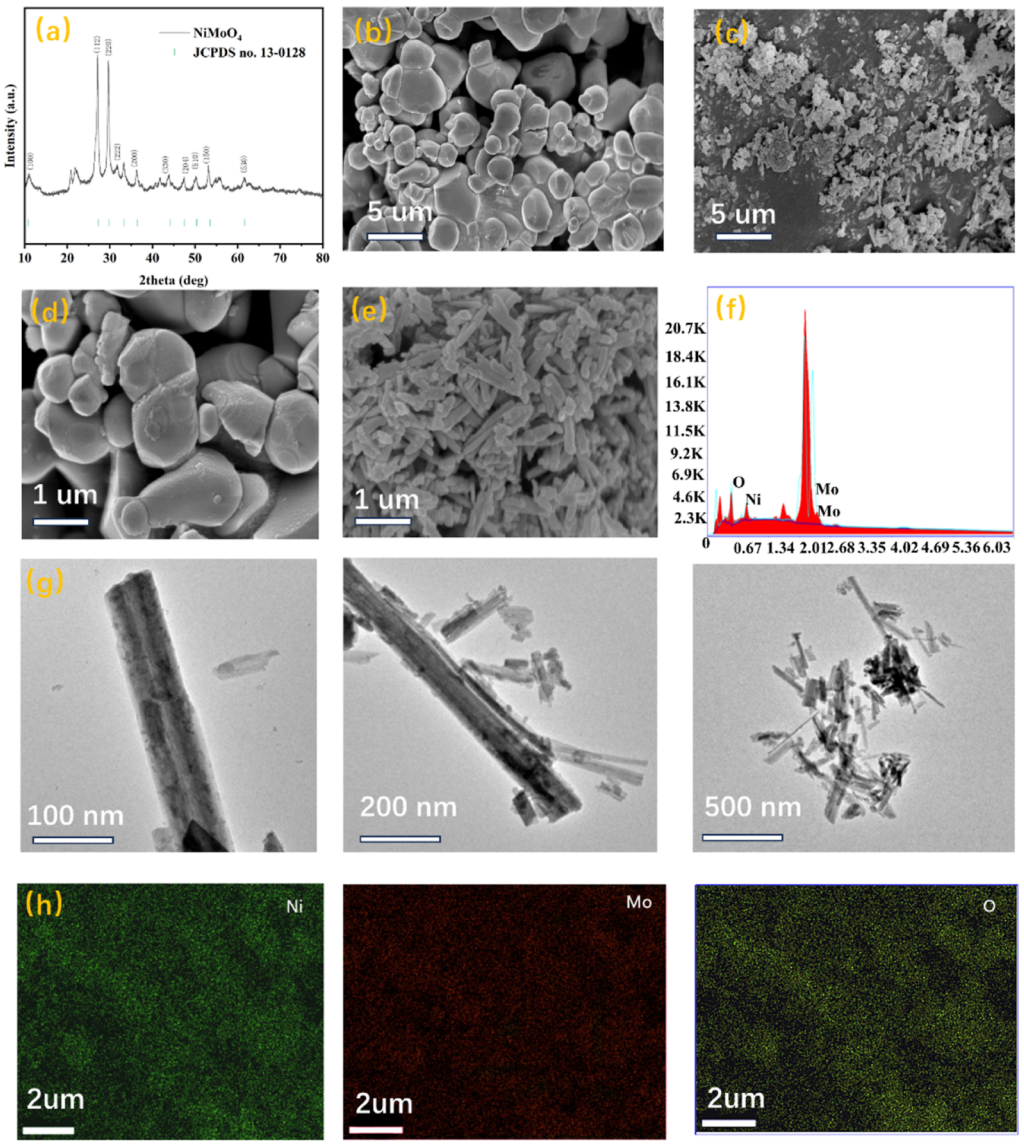

Figure 2. (a) XRD patterns of apparent $NiMoO_4$, (c,e) scanning electron microscopy (SEM) of $NiMoO_4$ and (b,d) NiO, (f) energy-dispersive spectrometry (EDS) of $NiMoO_4$, (g) transmission electron microscopy (TEM) of $NiMoO_4$, and (h) elemental mapping.

https://doi.org/10.1021/acsomega.3c09561
ACS Omega 2024, 9, 16118−16127

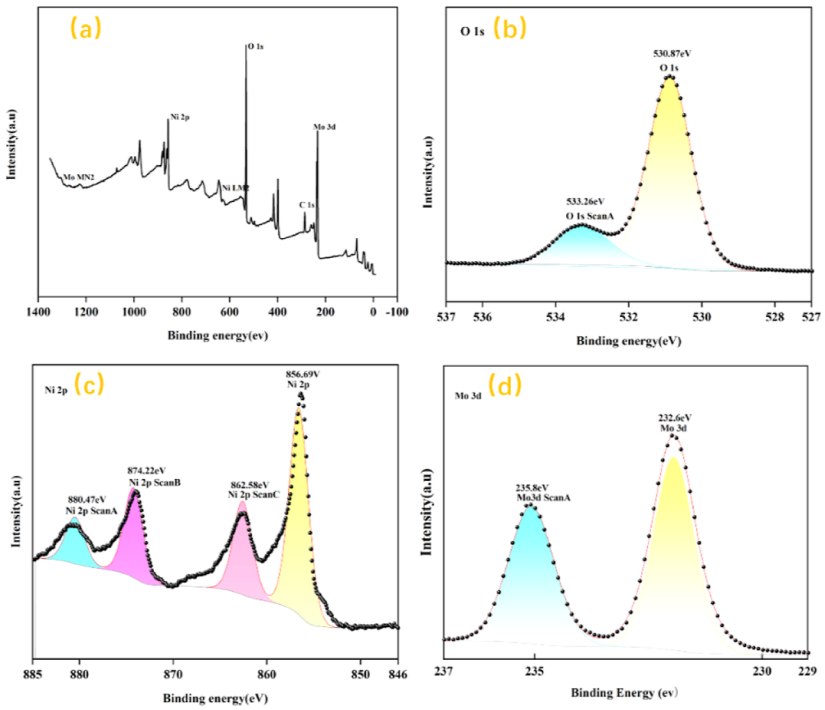

Figure 3. XPS of $NiMoO_4$ sample (a) survey spectra and high-resolution spectra of (b) O 1 s, (c) Ni 2p, and (d) Mo 3d.

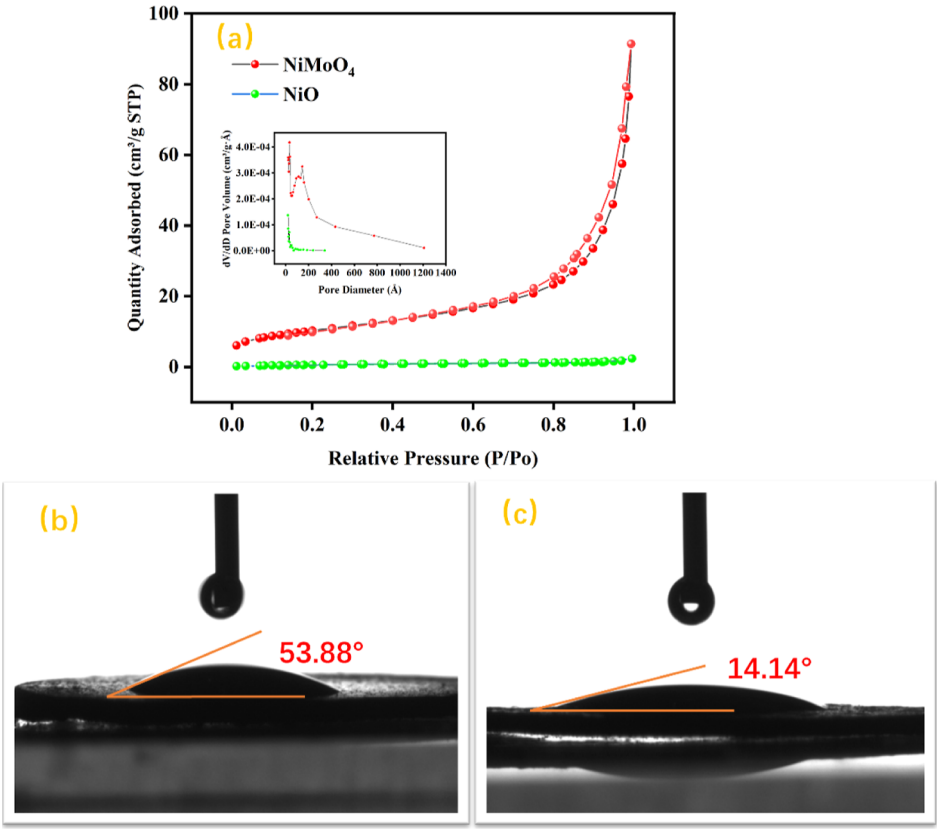

Figure 4. (a) Nitrogen adsorption−desorption isotherm and (b,c) KOH contact angle of the NiO and $NiMoO_4$.

2. EXPERIMENTAL SECTION

2.1. Material Synthesis of $NiMoO_4$. A schematic representation of the synthesis of $NiMoO_4$ is shown in Figure 1. All of our experiments utilized analytical-grade reagents, eliminating the need for additional purification. The solution was prepared by vigorously stirring a combination of 20 mL of water containing 0.75 g of polyvinylpyrrolidone (M_w = 40,000), 0.005 moles of $Ni(NO_3)_2{\cdot}6H_2O$, and 0.005 moles of $Na_2MoO_4{\cdot}7H_2O$ for a duration of 20 min. To enhance the dispersion of solution molecules, strong ultrasonication was applied for half an

https://doi.org/10.1021/acsomega.3c09561
ACS Omega 2024, 9, 16118−16127

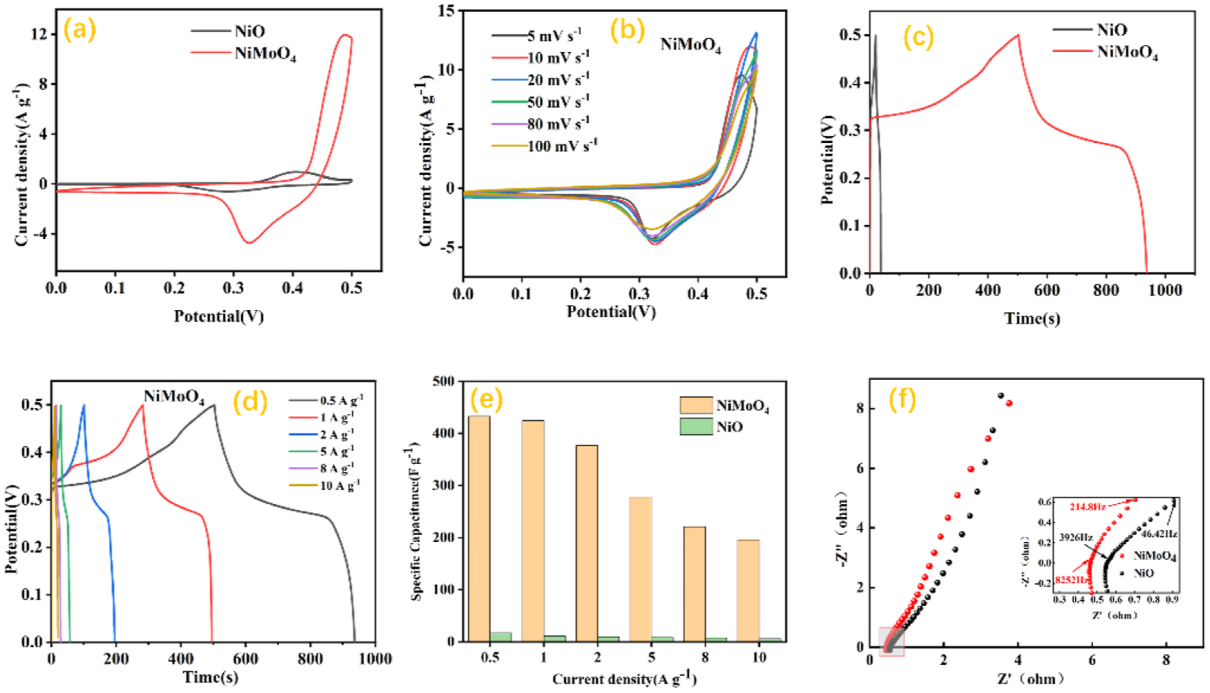

Figure 5. Electrochemical measurements of NiO and $NiMoO_4$ in 6 M KOH. (a) Comparison of CV curves at the scan rate of 10 mV s^{-1}, (b) CV plots at different scan rates, (c) GCD curves at the current density of 1 A g^{-1}, (d) GCD plots at different current densities of $NiMoO_4$, (e) specific capacitance at various current densities, and (f) electrochemical impedance spectroscopy (EIS) curves of NiO and $NiMoO_4$.

hour. Next, the prepared mixture was sealed and subjected to heating at a temperature of 150 °C for a duration of 6 h. Afterward, the resultant sample was obtained once it had cooled, and subsequently, it underwent a thorough cleansing using water and ethanol on multiple occasions, and then was dried in a vacuum at 60 °C for overnight. The NiO reagent was used for comparison.

2.2. Materials Characterizations and Electrochemical Measurements. This part can be found in Supporting Information for details.

3. RESULTS AND DISCUSSION

3.1. Structural and Morphological Study. The X-ray diffraction (XRD) analysis of the internal composition of the material is shown in Figure 2a. The XRD graphs indicate that the peaks of the fabricated $NiMoO_4$ nanorods precisely matched the distinctive peaks of the reference standard card in the database (PDF#13-0128). The (100), (112), (220), (222), (200), (330), (204), (510), (150), and (530) crystal plane families were responsible for the diffraction peaks observed at 10.92, 27.12, 29.62, 31.8, 36.36, 43.86, 47.34, 50.3, 53.18, and 61.6°, confirming the formation of $NiMoO_4$.

The SEM, EDS, and TEM analyses were performed to examine the morphological structure of the active material on the surface (Figure 2b−h). Figure 2c,e displays SEM images of the composites containing $NiMoO_4$. Upon comparison with NiO (b,d), it was observed that there has been a significant alteration in morphogenesis. $NiMoO_4$ exhibits rodlike structures in SEM images, whereas NiO exhibits a spherical structure. A $NiMoO_4$ nanorod with a diameter between 60 and 100 nm is shown in Figure 2e. The TEM image (Figure 2g) displays numerous nanorods attached to each other, which confirmed the availability of the one-pot hydrothermal strategy. Figure 2f,h shows the images depicting the elemental mapping of $NiMoO_4$. The composite samples have an equal distribution of Ni, Mo, and O.

Figure 3a−d illustrates the determination of the chemical composition and electronic states of the composite material using X-ray photoelectron spectroscopy (XPS). Figure 3a confirms the presence of Ni, Mo, and C without any additional impurities. The as-prepared sample is composed of Mo, C, O, and Ni, as evidenced by the six peaks at 1301.16, 856.69, 644, 530.87, 284.1, and 232.6 eV, corresponding to the Mo MN2, Ni 2p, Ni LM2, O 1s, C 1s, and Mo 3d levels, respectively. Figure 3b shows that the compound could be separated into two oxygen species, with the O 1s peak (530.87 eV) representing a typical metal−oxygen bond and the O 1s ScanA peak (533.26 eV) showing the physicochemical adsorption of water on the surface. The Ni 2p core level spectrum is shown in Figure 3c. The third part illustrates two types of Ni species that have Ni^{2+} peaks at 856.69, 880.47 eV and Ni^{3+} peaks at 862.58 and 874.22 eV, along with two additional shakeup satellites.[33] In Figure 3d, the Mo3d spectrum is displayed, and the peaks are separated into two distinct peaks. According to,[34] the Mo 3d and Mo 3d peaks were identified at 232 and 235.8 eV.

The measurement utilizing Brunauer−Emmett−Teller (BET) was conducted (Figure 4a) to further investigate the permeable arrangement in $NiMoO_4$ and NiO·$NiMoO_4$ surface area (36.99 m^2 g^{-1}) is greater than that of NiO surface area (2.66 m^2 g^{-1}) (Table S1), which provides a significant advantage in terms of facilitating rapid electron transfer and ion diffusion because of its superior structure. Moreover, the $NiMoO_4$ sample experiences a significant reduction in KOH contact angle, dropping from 53.88 to 14.14° following KOH activation. Figure 4b−c shows an enhancement in both surface wetness and electrolyte availability for the $NiMoO_4$ specimen.

3.2. Electrochemical Performance of NiO and $NiMoO_4$. The electrochemical characteristics of the two specimens were evaluated in a three-electrode setup using 6 M KOH as the

https://doi.org/10.1021/acsomega.3c09561
ACS Omega 2024, 9, 16118−16127

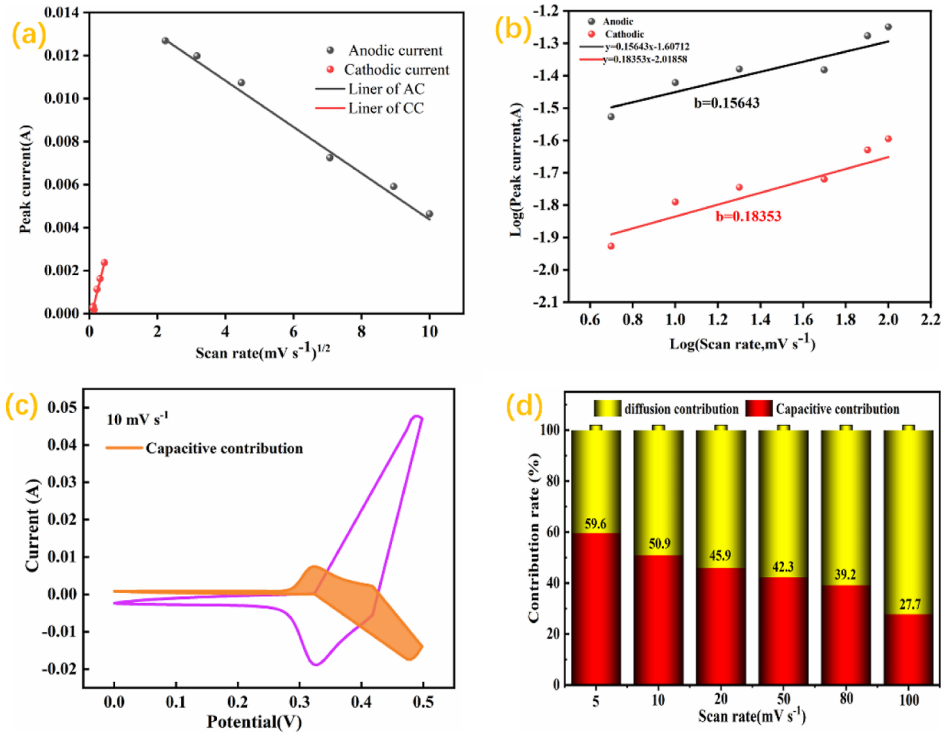

Figure 6. (a) Plots of anodic and cathodic peak currents of $NiMoO_4$ electrode as a function of the square root of sweep rates, (b) plots of log(peak current, i) vs log(scan rate, v), (c) capacitance-confined(orange region) and diffusion-controlled (blue region) contribution to charge storage of $NiMoO_4$ electrode at 10 mV s^{-1}, and (d) relative contribution of capacitance.

electrolytic solution. At different scanning speeds, the cyclic voltammetry (CV) plots of the original NiO and $NiMoO_4$ were initially investigated within the potential range of 0 to 0.5 V. Figure 5a shows the CV profiles of the two samples at a scan rate of 10 mV s^{-1}. Remarkably, the Faradaic oxidation−reduction reactions controlled separate oxidation−reduction peaks. $NiMoO_4$ has a higher current density and larger overall area than pure NiO. This implies that the specific capacitance of $NiMoO_4$ is expected to be greater owing to the presence of Mo. Additionally, Figure 5b presents comprehensive CV curves, illustrating the increase in the scan rate from 5 to 100 mV s^{-1}. Low resistance levels, rapid redox reaction rates, and high current densities were observed in the redox peaks as the scan rates increased.[35] The excellent balance between these curves demonstrates the strong reversibility.[36]

The electrochemical performance was evaluated by simultaneous GCD and CV evaluations. At a current density of 1 A g^{-1}, the GCD curves of NiO and $NiMoO_4$ (Figure 5c) exhibit contrasting dissimilarities. It is clear that $NiMoO_4$ has a longer charge/discharge time, which confirms its higher specific capacitance.[37] At 1 A g^{-1}, $NiMoO_4$ exhibits a significantly higher calculated Cs of 424.8 F g^{-1} compared to the Cs of pristine NiO of only 11 F g^{-1}. Figure 5d shows a nonlinear GCD curve at various current densities, further demonstrating their remarkable pseudo capacitance behavior.[38] The Cs (as shown in Figure 5e) values of pristine NiO and $NiMoO_4$ are 11 and 424.8 F g^{-1} at 1 A g^{-1}, respectively, while at 10 A g^{-1}, they are 6 and 196 F g^{-1}, respectively, as determined from the GCD curves, demonstrating the superiority of $NiMoO_4$ electrodes at high current densities because of their high Cs. The excellent performance of the $NiMoO_4$ electrode is primarily attributed to the following factors: (i) the atomic ratios of Ni^{2+}/Ni^{3+} and Mo^{2+}/Mo^{3+} are increased through chemical reduction, leading to highly reversible redox reactions and a greater capacity for electrochemical charge storage;[39−41] (ii) an increased oxygen content improves Cs, enhances conductivity, and facilitates rapid ion and electron transport by offering more electroactive sites.[42]

EIS measurements were performed to analyze the resistance of the samples (as shown in Figure 5f). In the high-frequency region, the x-axis intercept denotes the identical series resistance (R_s), the semicircle size corresponds to the charge transfer resistance (R_{ct}), and the slope of the low-frequency line represents the resistivity of ions diffusing at the electrode−electrolyte interface. The values of R_s and R_{ct} for $NiMoO_4$ were comparable to those of NiO. In the low-frequency range, $NiMoO_4$ shows a sharper inclination than NiO, suggesting a higher capacitance.[43−45] In particular, $NiMoO_4$ did not show an apparent semicircle in the high-frequency region, demonstrating an almost negligible surface charge transfer resistance.[46,47] Moreover, the greater slope of $NiMoO_4$ compared with that of NiO indicates a faster ion diffusion rate and reduced resistance to electrolyte diffusion. This can be attributed to the distinctive nanorod structure and the enhanced conductivity resulting from the oxygen content. Therefore, the EIS examination additionally verifies that $NiMoO_4$ demonstrates a reaction speed that is better than that of NiO when utilized as a supercapacitor electrode.

The kinetic behavior of the $NiMoO_4$ electrode was examined to evaluate the relationship between the fraction of peak current (i) and the square root of the scan rate ($v^{1/2}$). The results of this examination are shown in Figure 6a. The results of fitting i versus $v^{1/2}$ indicate a strong linear correlation, indicating that $NiMoO_4$ exhibits battery-like behavior and stores charges through diffusion-controlled reactions with the electrolytes.[48−50] To further evaluate the reaction kinetics and charge storage

https://doi.org/10.1021/acsomega.3c09561
ACS Omega 2024, 9, 16118−16127

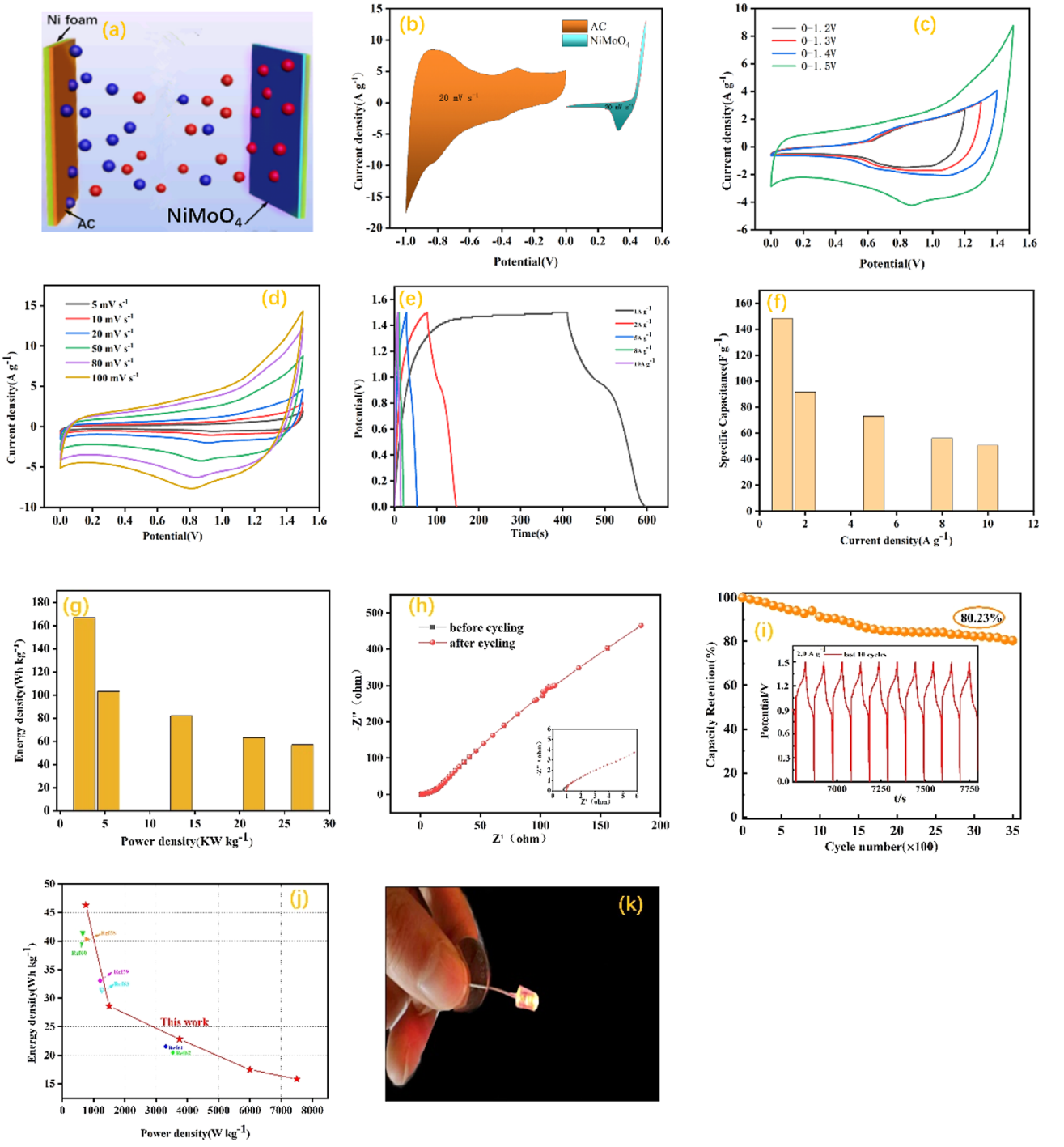

Figure 7. Electrochemical performance of the $NiMoO_4$//AC ASC device: schematic diagram representing the module of the ASC device (a), CV curves of the as-fabricated negative (AC, yellow region) and positive ($NiMoO_4$, blue region) electrode at the scan rate of 20 mV s^{-1} (b), CV profiles at diverse potential ranges at 50 mV s^{-1} (c), CV profiles at different scan rates (d), GCD profiles at different current densities (e), Cs at different current densities (f), energy density at different power density(g), EIS curves(h), cyclic performance of the device at 2 A g^{-1} (i), and Ragone plot of $NiMoO_4$// AC(j), powering a light-emitting diode light using a $NiMoO_4$//AC SC device (k).

mechanism of the $NiMoO_4$ electrode, the power law equation[51] was employed to demonstrate the relationship between the current peak (i) and the scan rate (v).

$$i = av^b \tag{1}$$

$$\log i = b \log v + \log a \tag{2}$$

where b and a represent the corresponding constants. Typically, the slope of the line corresponds to the b coefficient, which can be obtained by plotting the logarithm of i against the logarithm of diffusion-limited and capacitance-controlled behavior are the two typical restricted values for b, typically represented by 0.5 and 1, respectively.[52] For part b, the anodic and cathodic peak currents in this case were 0.15643 and 0.18353, respectively (Figure 6b). The presence of diffusion-controlled behavior is indicated, whereas the charge transfer process demonstrates a predominantly diffusion-controlled nature owing to the close

https://doi.org/10.1021/acsomega.3c09561
ACS Omega 2024, 9, 16118−16127

proximity of the b values to 0.5. To assess the impact of diffusion/capacitance on the total capacitance, the current response at a particular potential (iv) can be divided into two parts: capacitance-induced current (k_1v) and diffusion-induced current ($k_2v^{1/2}$), as explained in the equation.[53]

$$i_v = k_1v + k_2v^{1/2} \quad (3)$$

$$i_v/v^{1/2} = k_1v^{1/2} + k_2 \quad (4)$$

Calculating the values of k_1 and k_2 involved plotting $iv/v^{1/2}$ against $v^{1/2}$. In summary, the ratio of the electrical flow can be supplied for both the diffusion-limited charge-storage process and capacitance. Figure 6c illustrates the CV profile of the $NiMoO_4$ electrode at a sweep rate of 10 mV s^{-1}. This profile is separated into two regions: the orange region represents the contribution from capacitance confinement, whereas the purple region represents the contribution from diffusion control. At a scanning speed of 5 mV/s, the effect of capacitance regulation on the overall effectiveness was only 0.54%. Furthermore, the proportions of capacitance-controlled involvement at different sweep rates (5, 10, 20, 50, 80, and 100 mV s^{-1}) were calculated as 1.08, 2.16, 5.4, 8.64, and 10.8% of the entire capacitance, respectively (as shown in Figure 6d). The prevalence of the diffusion-restricted mechanism in the general electrochemical performance is apparent based on the findings acquired at different sweep rates. $NiMoO_4$'s rapid redox reaction rate can be attributed to the combination of capacitance-controlled and diffusion-confined contributions.

The construction of the $NiMoO_4$//AC ASC device is illustrated in Figure 7a. The ASC device was fabricated by using $NiMoO_4$ and AC in a 6 M KOH solution with a separator made of cellulose paper. Figure 7b shows the CV curves of $NiMoO_4$ and AC electrodes at a scanning rate of 20 mV s^{-1}. The $NiMoO_4$ electrode demonstrated electrochemical performance with a potential range of approximately 0−0.5 V, whereas the AC electrode displayed a potential range of −1 to 0. Consequently, the ASC device reached a maximum operational capacity of 1.5 V. In Figure 7b, the CV profiles of the ASC device are shown for different potential windows at a scan rate of 50 mV s^{-1}. It is evident from Figure 7c that the CV profile becomes distorted at 1.5 V due to the effects of oxygen evolution and polarization. Figure 7d illustrates the ASC device with an optimized potential window between 0 and 1.5 V. The CV profiles of the ASC device are shown at different sweep rates, with a voltage of 1.5 V. No significant distortion is observed across scan rates of 5−100 mV s^{-1} in all curves. Figure 7e demonstrates the impressive electrochemical reversibility and outstanding Coulombic efficiency of the ASC device, as indicated by the symmetrical GCD curves obtained at various current densities ranging from 1 to 10 A g^{-1}. Figure 7f shows the Cs values of the ASC apparatus at different current densities. The Cs value of the device is determined to be 41.17 mA h g^{-1} at 1 A g^{-1}. Figure 7g illustrates that the energy density can reach 46.3125 W h kg^{-1} at a power density of 0.75 kW kg^{-1}, and it remains at 15.833 W h kg^{-1} when the power density is 7.5 kW kg^{-1}. Moreover, there is no significant change in the EIS plots of the electrodes (Figure 7h). This finding is attributed to the excellent intrinsic conductivity and low charge transfer resistance of our special nanostructures.[18,19] The cycling capability of the ASC device was examined at a current density of 2 A g^{-1}, as shown in Figure 7i. After 3500 cycles, the ASC($NiMoO_4$//AC) device maintains a high capacitance retention of approximately 80.23%, indicating long cycle stability. The initial phase may experience a significant decrease in capacity loss owing to issues with the coating process and detachment of the electrode material during cycle testing.[54] Controlling the modes of forming composite could be a powerful strategy to improve the electrochemical performance for the composite materials.[55,56] Additionally, the degradation of $NiMoO_4$ also contributes to the decrease in capacitance during the initial cycle testing phase.[57]

In Figure 7j, the Ragone plot demonstrates that the supercapacitors achieve a maximum energy density of 46.3125 W h kg^{-1} when operated at a power density of 0.75 kW kg^{-1}. The performance of this $NiMoO_4$//AC ASC device is significantly superior to that of previously documented symmetrical and asymmetrical supercapacitors (as shown in Table S2), such as $NiMoO_4$/graphene(40.1 W h kg^{-1}),[58] $NiMoO_4/Fe_2O_3$(33.2 W h kg^{-1}),[59] MWCNTs/$NiMoO_4$(40.9 W h kg^{-1}),[60] NG/$NiMoO_4$//AC(22.2 W h kg^{-1}),[61] NiO@C15//CAC(21.6 W h kg^{-1}),[62] and $CoMoO_4$//pureG(31.61 W h kg^{-1}).[63] Furthermore, the prepared devices were connected to the diodes. Figure 7k illustrates that the devices are capable of illuminating red LEDs, which are commonly used in commercial lighting. This clearly shows immense possibilities for practical use.

4. CONCLUSIONS

In summary, $NiMoO_4$ materials with nanorod-like structures were produced using a straightforward and convenient one-step hydrothermal technique; at a current density of 1 A g^{-1}, the $NiMoO_4$ nanorods significantly enhanced the capacitance from 11 F g^{-1} (NiO) to 424.8 F g^{-1}. The device demonstrated stability over 3500 GCD cycles, maintaining 80.2% of its capacitance, thanks to its high-energy density of 46.3125 W h kg^{-1} and power density of 0.75 kW kg^{-1}. Compared with other nanostructured $NiMoO_4$ materials, $NiMoO_4$ nanorods offer rapid electron and ion transport. This superior electrochemistry shows that we present a simple one-step synthesis strategy for nanoscale bimetallic oxides applied to supercapacitors.

■ ASSOCIATED CONTENT

Data Availability Statement

Data will be made available on request.

Supporting Information

The Supporting Information is available free of charge at https://pubs.acs.org/doi/10.1021/acsomega.3c09561.

Calculations of the capacitances, energy density, and power density; materials characterizations; electrochemical measurements; Brunauer−Emmett−Teller for NiO and $NiMoO_4$; and energy density of the $NiMoO_4$//AC ASC device comparison to prior research (PDF)

■ AUTHOR INFORMATION

Corresponding Authors

Huixin Jin − *College of Material and Metallurgy, Guizhou University, Guiyang, Guizhou 550025, PR China;* orcid.org/0000-0002-2714-3445; Email: hxjin@gzu.edu.cn

Yi Wang − *College of Chemistry and Material Engineering, Guiyang University, Guiyang, Guizhou 550005, PR China;* Email: wy742011@hotmail.com

https://doi.org/10.1021/acsomega.3c09561
ACS Omega 2024, 9, 16118−16127

Authors

Meilong Wang − *College of Material and Metallurgy, Guizhou University, Guiyang, Guizhou 550025, PR China*

Linsong Li − *College of Material and Metallurgy, Guizhou University, Guiyang, Guizhou 550025, PR China*

Zhentao Liu − *College of Material and Metallurgy, Guizhou University, Guiyang, Guizhou 550025, PR China*

Fuzhong Wu − *College of Material and Metallurgy, Guizhou University, Guiyang, Guizhou 550025, PR China;* orcid.org/0000-0002-2486-6605

Complete contact information is available at: https://pubs.acs.org/10.1021/acsomega.3c09561

Notes

The authors declare no competing financial interest.

■ ACKNOWLEDGMENTS

We acknowledge financial support from the National Natural Science Foundation of China (22269003, 52164036, and U1960201); Guizhou Key Laboratory of Advanced Low-Dimensional Green Energy Storage Materials in Universities[2022]056; the central government guides local science and technology development funds [2022]4053; The Natural Science Research Project of Guizhou Provincial Department of Education [2022]041; and the Research and Innovation Team for Water Ion Battery Materials in Higher Education Institutions in Guizhou Province[2023]081.

■ REFERENCES

(1) Bonaccorso, F.; Colombo, L.; Yu, G.; Stoller, M.; Tozzini, V.; Ferrari, A. C.; Ruoff, R. S.; Pellegrini, V. Graphene, related two-dimensional crystals, and hybrid systems for energy conversion and storage. *Science* **2015**, *347*, 1246501.

(2) Choudhary, N.; Li, C.; Moore, J.; Nagaiah, N.; Zhai, L.; Jung, Y.; Thomas, J. Asymmetric supercapacitor electrodes and devices. *Adv. Mater.* **2017**, *29*, 1605336.

(3) Zhang, L. L.; Zhao, X. S. Carbon-based materials as supercapacitor electrodes. *Chem. Soc. Rev.* **2009**, *38*, 2520−2531.

(4) Hou, R.; Miao, M.; Wang, Q.; Yue, T.; Liu, H.; Park, H. S.; Qi, K.; Xia, B. Y. Integrated conductive hybrid architecture of metal-organic framework nanowire array on polypyrrole membrane for all-solid-state flexible supercapacitors. *Adv. Energy Mater.* **2019**, *10*, 1901892.

(5) Wang, L.; Ouyang, Y.; Jiao, X.; Xia, X.; Lei, W.; Hao, Q. Polyaniline-assisted growth of MnO2 ultrathin nanosheets on graphene and porous graphene for asymmetric supercapacitor with enhanced energy density. *Chem. Eng. J.* **2018**, *334*, 1−9.

(6) Jha, S.; Mehta, S.; Chen, Y.; Ma, L.; Renner, P.; Parkinson, D. Y.; Liang, H. Design and synthesis of lignin-based flexible supercapacitors. *ACS Sustain. Chem. Eng.* **2020**, *8*, 498−511.

(7) Liu, W.; Zhang, Z.; Zhang, Y.; Zheng, Y.; Liu, N.; Su, J.; Gao, Y. Interior and exterior decoration of transition metal oxide through Cu^0/Cu^+ co-doping strategy for high-performance supercapacitor. *Nano-Micro Lett.* **2021**, *13*, 61.

(8) Liu, S.; Kang, L.; Hu, J.; Jung, E.; Henzie, J.; Alowasheeir, A.; Zhang, J.; Miao, L.; Yamauchi, Y.; Jun, S. C. Realizing Superior Redox Kinetics of Hollow Bimetallic Sulfide Nanoarchitectures by Defect-Induced Manipulation toward Flexible Solid-State Supercapacitors. *Small* **2022**, *18*, No. e2104507.

(9) Xiao, D.; Dou, Q.; Zhang, L.; Ma, Y.; Shi, S.; Lei, S.; Yu, H.; Yan, X. Optimization of organic/water hybrid electrolytes for high-rate carbon-based supercapacitor. *Adv. Funct. Mater.* **2019**, *29*, 1904136.

(10) Hao, Q.; Xia, X.; Lei, W.; Wang, W.; Qiu, J. Facile synthesis of sandwich-like poly- aniline/boron-doped graphene nano hybrid for supercapacitors. *Carbon* **2015**, *81*, 552−563.

(11) Zhang, S.-W.; Yin, B.-S.; Liu, X.-X.; Gu, D.-M.; Gong, H.; Wang, Z.-B. A high energy density aqueous hybrid supercapacitor with widened potential window through multi approaches. *Nano Energy* **2019**, *59*, 41−49.

(12) Cui, X.; Chen, X.; Zhang, W.; Yan, X.; Wang, M.; Lian, J.; Zheng, Z.; Deng, H. Developing a facile method to construct 3D hierarchical CoMoO4@C@MnO2core-shell structure aligned on Ni foam with-enhanced pseudocapacitive performances. *J. Alloy. Compd.* **2017**, *695*, 2109−2116.

(13) Qian, Y.; Feng, J.; Xu, R.; Fan, D.; Du, Y.; Ren, X.; Wei, Q.; Ju, H. Zinc and molybdenum co-doped BiVO4 nanoarray for photo-electrochemical diethylstilbestrol analysis based on the dual-competitive system of manganese hexacyanoferrate hydrate nanocubes. *ACS Appl. Mater. Interfaces* **2020**, *12*, 16662−16669.

(14) Ouyang, Y.; Ye, H.; Xia, X.; Jiao, X.; Li, G.; Mutahir, S.; Wang, L.; Mandler, D.; Lei, W.; Hao, Q. Hierarchical electrodes of $NiCo_2S_4$ nanosheets-anchored sulfur-doped Co_3O_4 nanoneedles with advanced performance for battery-supercapacitor hybrid devices. *J. Mater. Chem. A* **2019**, *7* (7), 3228−3237.

(15) Yang, H.-X.; Zhao, D.-L.; Meng, W.-J.; Wu, Y.-Q.; Yang, Y.; Pu, H.; Gao, R.-Z. Facile synthesis of yolk-shelled NiO/Ni composites as cathode material for high-per-formance hybrid supercapacitors. *J. Power Sources* **2019**, *438*, 226977.

(16) Zhang, M.; Wang, Y.; Pan, D.; Li, Y.; Yan, Z.; Xie, J. Nitrogen-doped 3D graphene/MWNTs nanoframework-embedded Co3O4 for high electrochemical performance supercapacitors. *ACS Sustain. Chem. Eng.* **2017**, *5*, 5099−5107.

(17) Yao, T.; Guo, X.; Qin, S.; Xia, F.; Li, Q.; Li, Y.; Chen, Q.; Li, J.; He, D. Effect of rGO Coating on Interconnected Co3O4 Nanosheets and Improved Supercapacitive Behavior of Co3O4/rGO/NF Architecture. *Nano-Micro Lett.* **2017**, *9*, 38.

(18) Liu, S.; Kang, L.; Zhang, J.; Jung, E.; Lee, S.; Jun, S. C. Structural engineering and surface modification of MOF-derived cobalt-based hybrid nanosheets for flexible solid-state supercapacitors. *Energy Storage Mater.* **2020**, *32*, 167−177.

(19) Liu, S.; Kang, L.; Hu, J.; Jung, E.; Zhang, J.; Jun, S. C.; Yamauchi, Y. Unlocking the Potential of Oxygen-Deficient Copper-Doped Co3O4 Nanocrystals Confined in Carbon as an Advanced Electrode for Flexible Solid-State Supercapacitors. *ACS Energy Lett.* **2021**, *6*, 3011−3019.

(20) Lv, Z.; Luo, Y.; Tang, Y.; Wei, J.; Zhu, Z.; Zhou, X.; Li, W.; Zeng, Y.; Zhang, W.; Zhang, Y.; Qi, D.; Pan, S.; Loh, X. J.; Chen, X. Editable supercapacitors with customizable stretchability based on mechanically strengthened ultralong MnO2 nanowire composite. *Adv. Mater.* **2018**, *30*, 1704531.

(21) Mary, A. J. C.; Bose, A. C. Surfactant assisted ZnCo2O4 nanomaterial for supercapacitor application. *Appl. Surf. Sci.* **2018**, *449*, 105−112.

(22) Wang, N.; Sun, B.; Zhao, P.; Yao, M.; Hu, W.; Komarneni, S. Electrodeposition preparation of NiCo2O4 mesoporous film on ultrafine nickel wire for flexible asymmetric supercapacitors. *Chem. Eng. J.* **2018**, *345*, 31−38.

(23) Guo, C.; Li, J.; Chu, Y.; Li, H.; Zhang, H.; Hou, L.; Wei, Y.; Liu, J.; Xiong, S. Unusual formation of NiCo2O4@MnO2/nickel foam/MnO2 sandwich as advanced electrodes for hybrid supercapacitors. *Dalton Trans.* **2019**, *48*, 7403−7412.

(24) Beemarao, M.; Kanagambal, P.; Ravichandran, K.; Rajeswaran, P.; Ashraf, I. M.; Chalapathi, U.; Park, Si-H. Hybrids of porous NiMoO4@Reduced graphene oxide composites for asymmetric supercapacitor applications. *Inorg. Chem. Commun.* **2023**, *153*, 110853.

(25) Zhang, M.; Song, Z.; Liu, H.; Ma, T. Biomass-derived highly porous nitrogen-doped graphene orderly supported NiMn2O4 nano-crystals as efficient electrode materials for asymmetricsupercapacitors. *Appl. Surf. Sci.* **2020**, *507*, 145065.

(26) Zhang, Y.; Chang, C.; Jia, X.; Huo, Q.; Gao, H.; Yan, J.; Zhang, A.; Ru, Y.; Mei, H.; Gao, K.; et al. Morphology-dependent NiMoO4/carbon composites for high performance supercapacitors. *Inorg. Chem. Commun.* **2020**, *111*, 107631.

(27) Babu, B.; Talluri, B.; Gurugubelli, T. R.; Kim, J.; Yoo, K. Effect of annealing environment on the photoelectrochemical water oxidation

and electrochemical supercapacitor performance of SnO2 quantum dots. *Chemosphere* **2022**, *286*, 131577.
(28) Yewale, M. A.; Kadam, R. A.; Kaushik, N. K.; Koduru, J. R.; Velhal, N. B.; Nakate, U. T.; Jadhavar, A. A.; Sali, N. D.; Shin, D. K. Interconnected plate-like NiCo2O4 microstructures for supercapacitor application. *Mater. Sci. Eng., B* **2023**, *287*, 116072.
(29) Barqi, J.; Masoudpanah, S. M.; Hasheminiasari, M.; Liu, X. Nanoribbon-like NiCo2O4/reduced graphene oxide nanocomposite for high-performance hybrid supercapacitor. *J. Alloys Compd.* **2023**, *930*, 167509.
(30) Hsiao, Y.-C.; Yu, H.-Y.; Lee, P.-Y.; Yougbaré, S.; Lin, L.-Y.; Wu, Y.-F. Facile synthesis of ammonium-decorated cobalt molybdenum fluoride as electroactive material of supercapacitor. *J. Energy Storage* **2022**, *56*, 106055.
(31) Wei, G.; Wang, C.; Zhao, X.; Wang, S.; Kong, F. Plasma-assisted synthesis of Ni4Mo/MoO2@ carbon nanotubes with multiphase-interface for high-performance overallwater splitting electrocatalysis. *J. Alloys Compd.* **2023**, *939*, 168755.
(32) Li, M.-X.; Xiao, B.; Zhao, Z.-Y.; Ma, Y.; Zhou, Y.-N.; Zhang, X.-Y.; Wang, F.-G.; Chai, Y.-M.; Dong, B. Morphology evolution regulation of dual-doped S, Fe-NiMoO4 microrods based on precipitation-dissolution equilibrium for oxygen evolution. *Fuel* **2023**, *336*, 126769.
(33) Li, D.; Gong, Y.; Zhang, Y.; Luo, C.; Li, W.; Fu, Q.; Pan, C. Facile synthesis of carbon nanosphere/NiCo2O4 core-shell sub-microspheres for high performance supercapacitor. *Sci. Rep.* **2015**, *5*, 12903.
(34) Mehrez, J. A. A.; Owusu, K. A.; Chen, Q.; Li, L.; Hamwi, K.; Luo, W.; Mai, L. HierarchicalMnCo2O4@NiMoO4 as free-standing core-shell nanowire arrays with synergistic effect for enhanced supercapacitor performance. *Inorg. Chem. Front.* **2019**, *6*, 857−865.
(35) Jiao, Y.; Pei, J.; Chen, D.; Yan, C.; Hu, Y.; Zhang, Q.; Chen, G. Mixed-metallic MOF based electrode materials for high performance hybrid supercapacitors. *J. Mater. Chem. A* **2017**, *5* (3), 1094−1102.
(36) Wang, G.; Jin, Z. Oxygen-vacancy-rich cobalt-aluminium hydrotalcite structures served as high-performance supercapacitor cathode. *J. Mater. Chem. C* **2021**, *9* (2), 620−632.
(37) Jiao, Y.; Hong, W.; Li, P.; Wang, L.; Chen, G. Metal-organic framework derived Ni/NiO micro-particles with subtle lattice distortions for high-performance electrocatalyst and supercapacitor. *Appl. Catal., B* **2019**, *244*, 732−739.
(38) Wang, X.; Kim, H.-M.; Xiao, Y.; Sun, Y.-K. Nanostructured metal phosphide-based materials for electrochemical energy storage. *J. Mater. Chem. A* **2016**, *4* (39), 14915−14931.
(39) Bu, N.; Xiang, J.; Loy, S.; Yang, W.-D.; Di, Y.-F.; Zhao, R.-D.; Wu, F.-F.; Ma, D.-M.; Li, M. T.; Li, J. Preparation of three-dimensional Co3O4@ NiMoO4 nanorods as electrode materials for supercapacitors. *Mater. Chem. Phys.* **2022**, *288*, 126419.
(40) Wang, P.; Ding, X.; Zhe, R.; Zhu, T.; Qing, C.; Liu, Y.; Wang, H.-E. Synchronous defect and interface engineering of NiMoO4 nanowire arrays for high-performance supercapacitors. *Nanomaterials* **2022**, *12*, 1094.
(41) Normohammadi, S.; Bahmani, F.; Fotouhi, L.; Khoshfetrat, M. Electrodeposited nickel nanocone/NiMoO4 nanocomposite designed as superior electrode materials for high performance supercapacitor. *Int. J. Hydrogen Energy* **2022**, *47*, 5220−5229.
(42) Dai, S.; Han, F.; Tang, J.; Tang, W. MOF-derived Co3O4 nanosheets rich in oxygen vacancies for efficient all-solid-state symmetric supercapacitors. *Electrochim. Acta* **2019**, *328*, 135103.
(43) Poudel, M. B.; Kim, H. J. Synthesis of high-performance nickel hydroxide nanosheets/gadolinium doped-α-MnO2 composite nanorods as cathode and Fe3O4/GO nanospheres as anode for an all-solid-state asymmetric supercapacitor. *J. Energy Chem.* **2022**, *64*, 475−484.
(44) Zhang, Z.; Mu, S.; Zhang, B.; Tao, L. . u.; Huang, S.; Huang, Y.; Gao, F.; Zhao, Y. A novel synthesis of carbon nanotubes directly from an indecomposable solid carbon source for electrochemical applications. *J. Mater. Chem. A* **2016**, *4* (6), 2137−2146.
(45) Zhu, Y.; Lu, P.; Li, F.; Ding, Y.; Chen, Y. Metal-Rich Porous Copper Cobalt Phosphide Nanoplates as a High-Rate and Stable Battery-Type Cathode Material for Battery-Supercapacitor Hybrid Devices. *ACS Appl. Energy Mater.* **2021**, *4* (4), 3962−3974.
(46) Yan, Y.; Lin, J.; Xu, T.; Liu, B.; Huang, K.; Qiao, L.; Liu, S.; Cao, J.; Jun, S. C.; Yamauchi, Y.; Qi, J. Atomic-Level Platinum Filling into Ni-Vacancies of Dual-Deficient NiO for Boosting Electrocatalytic Hydrogen Evolution. *Adv. Energy Mater.* **2022**, *12*, 2200434.
(47) Yan, Y.; Lin, J.; Huang, K.; Zheng, X.; Qiao, L.; Liu, S.; Cao, J.; Jun, S. C.; Yamauchi, Y.; Qi, J. Tensile Strain-Mediated Spinel Ferrites Enable Superior Oxygen Evolution Activity. *J. Am. Chem. Soc.* **2023**, *145*, 24218−24229.
(48) Li, S.; Hua, M.; Yang, Y.; Huang, W.; Lin, X.; Ci, L.; Lou, J.; Si, P. Self-supported multidimensional Ni−Fe phosphide networks with holey nanosheets for high- performance all-solid-state supercapacitors. *J. Mater. Chem. A* **2019**, *7* (29), 17386−17399.
(49) Huang, B.; Wang, H.; Liang, S.; Qin, H.; Li, Y.; Luo, Z.; Zhao, C.; Xie, L. . i.; Chen, L. Two-dimensional porous cobalt−nickel tungstate thin sheets for high performance supercapattery. *Energy Storage Mater.* **2020**, *32*, 105−114.
(50) Wang, Y.; Song, Y.; Xia, Y. Electrochemical capacitors: mechanism, materials, systems, characterization and applications. *Chem. Soc. Rev.* **2016**, *45* (21), 5925−5950.
(51) Acharya, J.; Ko, T. H.; Seong, J.-G.; Seo, M.-K.; Khil, M.-S.; Kim, H.-Y.; Kim, B.-S. Hybrid Electrodes Based on Zn−Ni−Co Ternary Oxide Nanowires and Nanosheets for Ultra-High-Rate Asymmetric Supercapacitors. *ACS Appl. Nano Mater.* **2020**, *3* (9), 8679−8690.
(52) Yan, J.; Ren, C. E.; Maleski, K.; Hatter, C. B.; Anasori, B.; Urbankowski, P.; Sarycheva, A.; Gogotsi, Y. Flexible MXene/Graphene Films for Ultrafast Supercapacitors with Outstanding Volumetric Capacitance. *Adv. Funct. Mater.* **2017**, *27* (30), 1701264.
(53) Zhang, M.; Chen, Z.; Wang, Y.; Zhang, J.; Zheng, X.; Rao, D.; Han, X.; Zhong, C.; Hu, W.; Deng, Y. Enhanced light harvesting and electron-hole separation for efficient photocatalytic hydrogen evolution over Cu7S4-enwrapped Cu2O nanocubes. *Appl. Catal., B* **2019**, *246*, 202−210.
(54) Zhang, A.; Zhang, H.; Hu, B.; Wang, M.; Zhang, S.; Jia, Q.; He, L.; Zhang, Z. The intergrated nanostructure of bimetallic CoNi-based zeolitic imidazolate framework and carbon nanotubes as high-performance electrochemical supercapacitors. *J. Colloid Interface Sci.* **2022**, *608*, 1257−1267.
(55) Yan, X.; He, Y.; Liu, X.; Jing, S.; Guan, J.; Gao, W.; Ray, S.; Xiong, Y.; Li, T.; Ge, X. Deterministic Effect of the Solid-State Diffusion Energy Barrier for a Charge Carrier on the Self-Discharge of Supercapacitors. *ACS Energy Lett.* **2023**, *8*, 2376−2384.
(56) Jing, S.; Yan, X.; Xiong, Y.; Li, T.; Xiong, J.; Hu, T.; Wang, Z.; Lou, L.; Ge, X. Regulating the synergy coefficient of composite materials for alleviating self-discharge of supercapacitors. *J. Energy Chem.* **2023**, *84*, 34−40.
(57) Wang, Y.-G.; Li, H.-Q.; Xia, Y.-Y. Ordered Whiskerlike Polyaniline Grown on the Surface of Mesoporous Carbon and Its Electrochemical Capacitance Performance. *Adv. Mater.* **2006**, *18* (19), 2619−2623.
(58) Zhang, Y.; Yao, Q.-Q.; Gao, H.-L.; Wang, L.-Z.; Jia, X.-L.; Zhang, A.-Q.; Song, Y.-H.; Xia, T.-C.; Dong, H.-C. Facile synthesis and electrochemical performance of manganese dioxide doped by activated carbon, carbon nanofiber and carbon nanotube. *Powder Technol.* **2014**, *262*, 150−155.
(59) Yang, J.; Liu, W.; Niu, H.; Cheng, K.; Ye, K. . e.; Zhu, K.; Wang, G.; Cao, D.; Yan, J. Ultrahigh energy density battery-type asymmetric supercapacitors: NiMoO4 nanorod-decorated graphene and graphene/Fe2O3 quantum dots. *Nano Res.* **2018**, *11*, 4744−4758.
(60) Yousefipour, K.; Sarraf-Mamoory, R.; Chaychi Maleki, A. A new strategy for the preparation of multi-walled carbon nanotubes/NiMoO4 nanostructures for high-performance asymmetric supercapacitors. *J. Energy Storage* **2023**, *59*, 106438.
(61) Feng, X.; Ning, J.; Wang, D.; Zhang, J. C.; Xia, M. Y.; Wang, Y.; Hao, Y. Heterostructurearrays of NiMoO4 nanoflakes on N-doping of graphene for high-performance asymmetric supercapacitors. *J. Alloy. Compd.* **2020**, *816*, 152625.

https://doi.org/10.1021/acsomega.3c09561
ACS Omega 2024, 9, 16118−16127

(62) Muduli, S.; Pati, S. K.; Pani, T. K.; Martha, S. K. One pot synthesis of carbon decorated NiO nanorods as cathode materials for high-performance asymmetric supercapacitors. *J. Energy Storage* **2023**, *66*, 107339.
(63) Sivakumar, P.; Justin, C.; Ramesh, R.; Loganathan, K.; JeongWon, P.; Hyun, J. Influence of heat-treatment temperature on the improvement of the electrochemical performance of CoMoO4 nanomaterials for hybrid supercapacitor application. *Ceram. Int.* **2022**, *48* (19), 29018−29024.

https://doi.org/10.1021/acsomega.3c09561
ACS Omega 2024, 9, 16118−16127